Research on Chemical Intermediates (2018) 44:6753–6763
https://doi.org/10.1007/s11164-018-3520-z

Entrapment of Bi_2O_3 nanoparticles in TiO_2 nanotubes for visible light-driven photocatalysis

Quanming Peng[1,3] · Guiming Peng[2] · Liangpeng Wu[1] · Xiaoyang Wang[1,3] · Xu Yang[1] · Xinjun Li[1]

Received: 12 April 2018 / Accepted: 18 June 2018 / Published online: 21 June 2018

Abstract

In this study, we prepared nanoparticles of the visible light-responsive photocatalyst, Bi_2O_3 entrapped in anatase TiO_2 nanotubes (Bi_2O_3-in-TNTs) via a vacuum-assisted precursor-filling process followed by annealing. Owing to the unique tubular electronic structure of TiO_2 nanotubes, the interior of the nanotube is in an electron-deficient state, which was confirmed by XPS spectra and H_2-TPR. Electrochemical impedance studies showed that the Bi_2O_3-in-TNTs demonstrated a more efficient separation of photogenerated carriers than when Bi_2O_3 nanoparticles were deposited on the outer wall of TiO_2 nanotubes (Bi_2O_3-out-TNTs). Due to the confinement effect of TiO_2 nanotubes, which inhibits photogenerated carriers' recombination, the Bi_2O_3-in-TNTs exhibited a better photocatalytic performance for the photo-degradation of methyl orange under visible light compared to Bi_2O_3-out-TNTs.

Keywords TiO_2 nanotubes · Bi_2O_3 · Confinement effect · Visible light · Photocatalysis

Electronic supplementary material The online version of this article (https://doi.org/10.1007/s11164-018-3520-z) contains supplementary material, which is available to authorized users.

✉ Xinjun Li
lixj@ms.giec.ac.cn

[1] Key Laboratory of Renewable Energy, Guangdong Provincial Key Laboratory of New and Renewable Energy Research and Development, Guangzhou Institute of Energy Conversion, Chinese Academy of Sciences (CAS), Guangzhou 510640, China

[2] School of Materials and Energy, Guangdong University of Technology, Guangzhou 510006, China

[3] University of Chinese Academy of Sciences, Beijing 100049, China

Introduction

Materials for efficient remediation of environmental pollution have attracted tremendous attention from chemists and material scientists [1–3]. Visible light photocatalytic technology is seen as a promising approach, especially in the use of solar energy for environmental treatment on wastewater [4, 5] and volatile organic compounds (VOCs) [6, 7]. A highly efficient photocatalyst should have good light harvesting and effective photogenerated electron–hole separation properties. The construction of p–n junctions between different semiconductors benefits charge separation and inhibits electron–hole recombination [8–10]. Bismuth oxide (Bi_2O_3) is a p-type visible light-active material with a bandgap of $\sim$ 2.8 eV [12]. Hybridizing TiO_2 with Bi_2O_3 has been reported to improve photocatalytic performance toward organic compound photodegradation [12–16].

Entrapping the active components in a confined space has been reported as an efficient strategy for enhancing catalytic activity. Bao et al. reported that the properties of Fe_2O_3 were modified significantly when Fe_2O_3 nanoparticles were encapsulated in carbon nanotubes (CNTs). In particular, the auto reduction of Fe_2O_3 is facilitated with CNT channels compared to the case when those nanoparticles are located on the CNT outer walls [17], and the reduction temperature decreases monotonically with the inner diameter of the CNTs [18]. They concluded that this enhancement of catalytic activity is attributable to the confinement effect [19]. Recently, our previous work also revealed that pure metal (i.e. Pd, Pt) or metal components (i.e. CdS, MnO_2) entrapped in TiO_2 nanotubes (TNTs) demonstrate remarkably enhanced catalytic activity towards hydrogenation [20, 21], Fisher-Tropsch synthesis [22], catalytic combustion [23, 24], and hydrogen production [25]. However, the behavior of a visible light-responsive photocatalyst confined by TNTs for photocatalytic degradation of organic compounds has not yet been reported.

In this report, Bi_2O_3 nanoparticles entrapped in anatase TNTs (Bi_2O_3-in-TNTs) were prepared via a vacuum-assisted precursor filling process followed by thermal calcination. Subsequently, we examined the differences in visible light-driven photocatalytic performance between Bi_2O_3-in-TNTs and similar Bi_2O_3 nanoparticles deposited on the outer wall of TNTs (Bi_2O_3-out-TNTs) by investigating the material structure, light absorption property, charge transfer property and degradation performance towards methyl orange (MO).

Experimental

Chemicals and materials

All chemicals were used as received without further purification. Sodium hydroxide (NaOH, $\geq$ 96%), hydrochloric acid (HCl, 36–38%), and bismuth nitrate ($Bi(NO_3)_3 \cdot 5H_2O$, $\geq$ 90.0%) were obtained from Guangzhou Chemical Reagent Inc. Glycerol ($\geq$ 99.0%) was purchased from Tianjin Fuyu Chemical Reagent Inc.

Material synthesis

Synthesis of TNTs

Anatase TNTs were synthesized via a hydrothermal method following procedures according to our previous report [26]. Firstly, 2 g of anatase TiO_2 powder were added into 100 mL 10 mol/L NaOH aqueous solution in a 250 mL Teflon-lined flask. After sealing, the reactor was heated at 110 °C under atmospheric pressure and magnetic stirring for 24 h. After cooling to room temperature, the white precipitate was neutralized by 0.1 mol/L HCl solution and was washed with deionized water. Finally, the TNTs were obtained by annealing at 250 °C for 2 h in ambient atmosphere.

Synthesis of Bi_2O_3-in-TNTs and Bi_2O_3-out-TNTs

Firstly, 1 g of TNTs were mixed with 4 mL $Bi(NO_3)_3$ solution by stirring for 2 h in a vacuum, while the $Bi(NO_3)_3$ solution was made by dissolving 1.04 g of $Bi(NO_3)_3{\cdot}5H_2O$ in 30 mL glycerol and 70 mL water. Here glycerol was used as co-solvent to promote the dissolution of $Bi(NO_3)_3{\cdot}5H_2O$. After that, the solution was heated at 60 °C to evaporate the solvent until a dry powder was obtained. The powder was subsequently calcinated at 350 °C for 2 h. Then the composite, TNTs filled with in situ grown Bi_2O_3 nanoparticles (Bi_2O_3-in-TNTs), was obtained. The theoretical content of Bi_2O_3 in the catalyst of Bi_2O_3-in-TNTs was 2.0 wt%. As an experimental control, Bi_2O_3 nanoparticles were grown on the outer wall of TNTs (Bi_2O_3-out-TNTs) following the same procedures but without vacuum pumping. Catalysts with different Bi_2O_3 deposition amounts were prepared by adjusting the concentration of $Bi(NO_3)_3{\cdot}5H_2O$ in the precursor solution.

Material characterizations

The morphology of the catalysts was inspected by field-emission scanning electron microscopy (FESEM, Hitachi S-4800). High resolution transmission electron microscopy (HRTEM) measurements were carried out using a JEM-2010HR microscope with an acceleration voltage of 200 kV. X-ray diffraction (XRD) patterns were collected on an X-ray diffractometry (X'Pert-PRO, PANalytical, Holland) equipped with Cu Ka radiation at an accelerating voltage of 40 kV. X-ray photoelectron spectroscopy (XPS) was performed on Thermo Fisher Scientific ESCALAB 250xi using monochromated Kα X-rays (1486.6 eV).

Electrochemical impedance spectroscopy (EIS) was measured in 0.1 mol/L Na_2SO_4 aqueous solution at a bias of 0.28 V by using a three-electrode system. An Ag/AgCl electrode was used as the reference electrode while the counter electrode was a Pt wire. The sample for EIS measurement was prepared via the doctor blade method. Firstly, 1 g of the obtained catalyst was dispersed in 2 mL ethanol. The mixture was then ground until a well dispersed milky-paste was obtained. Secondly, the paste was coated onto FTO glass via the doctor blade method. Then, the obtained film was dried at 60 °C to evaporate the ethanol. The film was

subsequently calcinated at 200 °C for 2 h to increase the adhesion. UV–Vis absorption spectra were obtained from a Shimadzu U3010 UV–Vis spectrophotometer. Hydrogen temperature-programmed reduction (H_2-TPR) experiments were performed on a CPB-1 (ChemBet, America) using H_2 (5% in Ar, v/v) as the testing gas with a flow of 50 mL/min.

Photo-degradation experiments

Firstly, a suspension of 10 mg of catalyst in 100 mL aqueous MO solution (20 ppm) was stirred for 30 min in a quartz reactor in dark conditions for adsorption–desorption equilibration. After that, MO photo-degradation was performed by using a metal halide lamp as the light source. The irradiation power intensity was 250 W. The degradation cell was maintained at ambient temperature by a water cooling system. During the whole degradation experiment, MO concentration was monitored by UV–Vis measurements.

Results and discussion

The TNTs, Bi_2O_3-in-TNTs and Bi_2O_3-out-TNTs were examined by TEM with the results shown in Fig. 1. From the results of TEM, it can be seen that one-dimensional nanotubes were obtained. For the pristine TNTs, the outer walls were smooth and clean (Fig. 1a). After a vacuum-assisted deposition, Bi_2O_3 nanoparticles were found to be successfully anchored onto the inner wall of the TNTs (Fig. 1b).

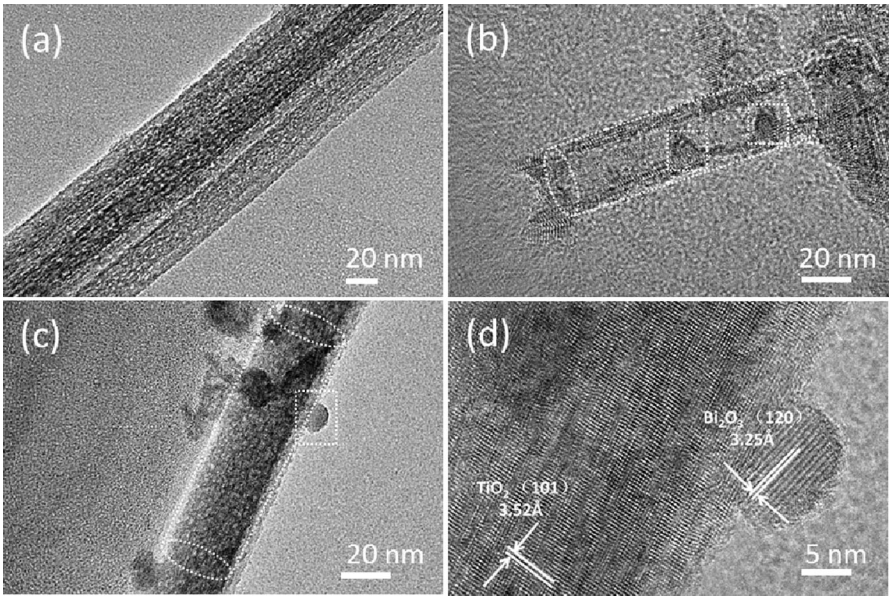

Fig. 1 **a** TEM image of bare TNTs; **b** TEM image of Bi_2O_3-in-TNTs; **c** TEM image Bi_2O_3-out-TNTs; **d** HRTEM image Bi_2O_3-out-TNTs

Samples prepared in ambient pressure showed the Bi_2O_3 nanoparticles grown on the outer wall of the nanotubes (Fig. 1c). The successful entrapment of Bi_2O_3 nanoparticles inside the TNTs is ascribed to the good filling of $Bi(NO_3)_3$ into the nanotubes by the pumping process. Lattice fringes with the interplanar spacing of 3.52 Å are indicative of the (101) plane of anatase TiO_2 while another diffraction fringes with the lattice interspacing of 3.25 Å can be assigned to the (120) plane of Bi_2O_3 (Fig. 1d) [27]. The confirmation of Bi_2O_3 implies that the calcination of 2 h at 350 °C successfully transformed the $Bi(NO_3)_3$ into oxide. Consistent with the TEM images, one dimensional nanostructures were observed by SEM, while the Bi_2O_3 nanoparticles were hardly discernable because of their small sizes (Figure S1). BET surface area results show that the deposition of Bi_2O_3 nanoparticles leads to a slight increase of surface area for both Bi_2O_3-in-TNTs and Bi_2O_3-out-TNTs (Figure S2 and Table S1). The pore size becomes relatively smaller after incorporation of Bi_2O_3 nanoparticles (Table S1).

XRD patterns of Bi_2O_3-in-TNTs and Bi_2O_3-out-TNTs are shown in Fig. 2. As can be seen, both patterns exhibit the same diffraction peaks at 25.41°, 37.93°, 48.17°, 54.02°, 55.13°, 62.76°, 69.08°, 70.18°, and 75.17°, which are well indexed to the (101) (004), (200), (105), (211), (204), (116), (220), and (301) planes of anatase TiO_2 (JCPDS card No. 21-1272). However, no characteristic peaks of Bi_2O_3 can be discerned, probably because of the low loading of Bi_2O_3 or hindrance by the strong TiO_2 peaks.

Figure 3 shows the XPS spectra of Bi_2O_3-in-TNTs and Bi_2O_3-out-TNTs. First of all, the presence of a Bi4f peak in the survey XPS spectra further confirms the growth of Bi_2O_3 nanoparticles on TNTs (Fig. 3a), while its relatively low peak intensity indicates a low loading of Bi_2O_3 nanoparticles. The weight ratio of Bi_2O_3 nanoparticles in Bi_2O_3-in-TNTs and Bi_2O_3-out-TNTs is 2.0 and 2.2 wt% as revealed by XPS (Table S2), respectively. O1s XPS spectra demonstrate a main lattice oxygen peak at 530 eV accompanied by a small shoulder weak peak at 532 eV, which is caused by the adsorbed oxygen (Fig. 3b). The peak at 459 eV in Ti 2p XPS spectra is attributed to the Ti–O–Ti bond (Fig. 3c). Bi4f XPS spectra

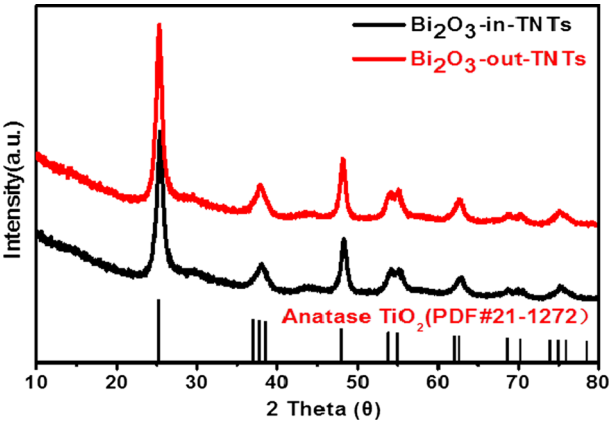

Fig. 2 XRD patterns of Bi_2O_3-in-TNTs and Bi_2O_3-out-TNTs

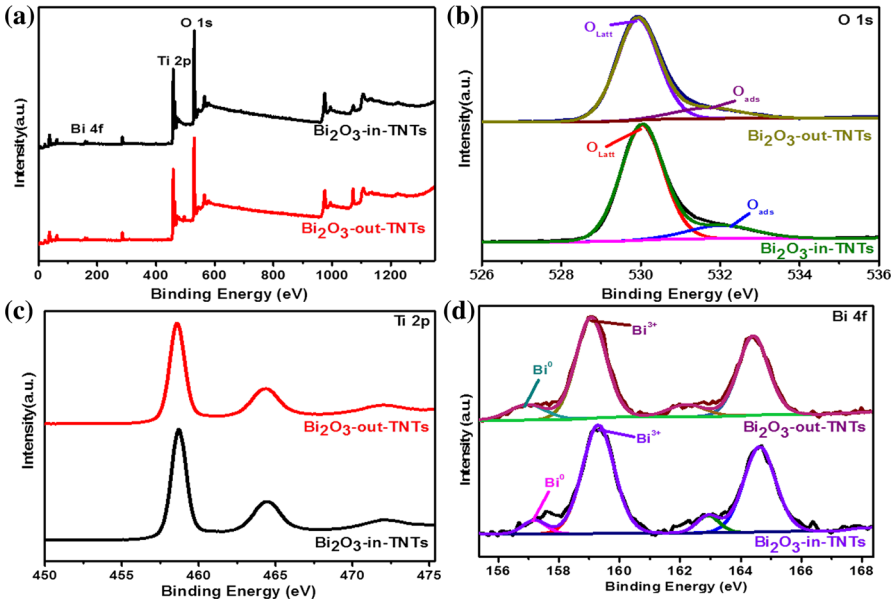

Fig. 3 **a** XPS survey spectra, **b** O1 s XPS spectra, **c** Ti 2p XPS spectra, and **d** Bi 4f XPS spectra of Bi_2O_3-in-TNTs and Bi_2O_3-out-TNTs

demonstrates a Bi4f spectra with two peaks located at 159 and 157 eV can be deconvoluted. These two peaks belong to the Bi^{3+} and Bi^0 species, respectively [13]. Interestingly, the Bi^{3+}/Bi^0 peak ratios of Bi_2O_3-in-TNTs and Bi_2O_3-out-TNTs differ greatly from each other (Table 1). The Bi^{3+}/Bi^0 ratio of Bi_2O_3-in-TNTs is almost double that of Bi_2O_3-out-TNTs (10.5 vs 5.4), indicating that the Bi species encapsulated inside TNTs prefer to exist in a more oxidative state. Similar findings have been reported on the Fe_2O_3 particles confined in TiO_2 nanotubes [22]. As a result, the high ratio of Bi^{3+}/Bi^0 inside the TNTs, theoretically, endows the inner surface of TNTs with an electron-deficient property.

To further prove the surface electron states of TiO_2 nanotubes, H_2-TPR experiments were performed with the results shown in Fig. 4. As shown, two prominent material reduction peaks sitting at ~ 330 and ~ 500 °C can be discerned for both Bi_2O_3-in-TNTs and Bi_2O_3-out-TNTs. The two reduction peaks can be attributed to the reduction of Bi^{3+} to metallic Bi. Importantly, there is a

Table 1 Bi 4f XPS spectra data of Bi_2O_3-in-TNTs and Bi_2O_3-out-TNTs

Catalysts	Species	BE/eV[a]	Atomic %	Bi^{3+}/Bi^0 ratio
Bi_2O_3-in-TNTs	Bi^{3+}	159.3	0.19173	10.5
	Bi^0	157.2	0.01827	
Bi_2O_3-out-TNTs	Bi^{3+}	159.1	0.19412	5.4
	Bi^0	157.0	0.03588	

[a]*BE* binding energy

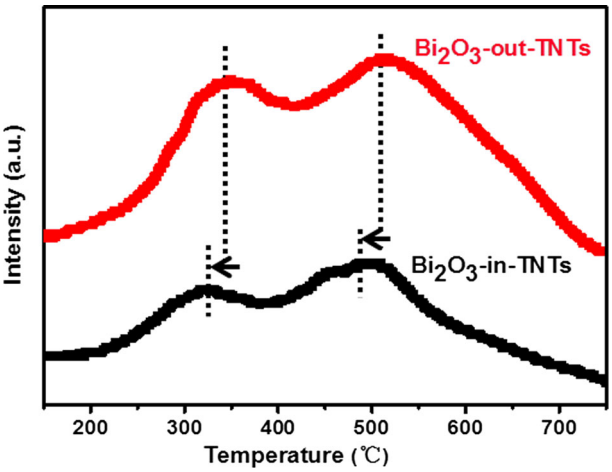

Fig. 4 H_2-TPR pattern of Bi_2O_3-in-TNTs and Bi_2O_3-out-TNTs

20 °C shift toward lower temperature for the two reduction peaks of Bi_2O_3-in-TNTs relative to that of Bi_2O_3-out-TNTs, which provides further evidence for the electron-deficiency at the inner surface of TNTs.

Figure 5 shows the UV–Vis absorption spectra of the bare TNTs, Bi_2O_3-out-TNTs, and Bi_2O_3-in-TNTs. Apparently, the TNTs exhibit a strong UV absorption. The two catalysts, Bi_2O_3-in-TNTs and Bi_2O_3-out-TNTs, exhibit absorption in the visible wavelength range due to the incorporation of Bi_2O_3. Meanwhile, the absorption edge of Bi_2O_3-in-TNTs is red-shifted compared to Bi_2O_3-out-TNTs, indicating that the TNTs exert a charge separation effect [28].

In order to study the electrochemical behaviors of Bi_2O_3-in-TNTs, charge transfer properties within the materials was investigated by EIS (Fig. 6). Obviously, the arc size for Bi_2O_3-in-TNTs in high frequency region is several-times smaller

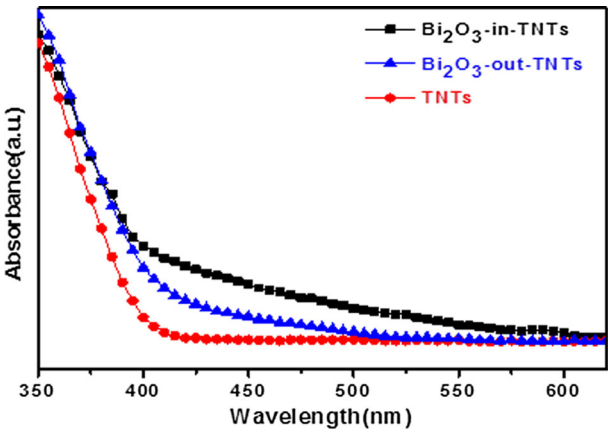

Fig. 5 UV–Vis absorption spectra of the Bi_2O_3-in-TNTs, Bi_2O_3-out-TNTs, and TNTs

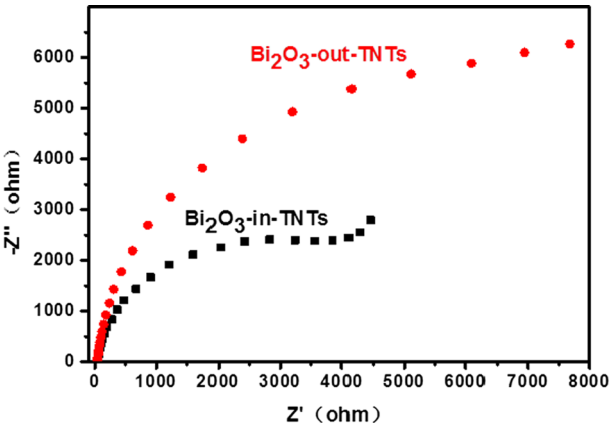

Fig. 6 The Nyquist plots of Bi_2O_3-in-TNTs and Bi_2O_3-out-TNTs catalysts in 0.1 mol/L Na_2SO_4 aqueous solution at 0.28 V (vs. Ag/AgCl)

compared to Bi_2O_3-out-TNTs, indicating the much smaller charge transfer resistance, and higher electron–hole separation efficiency. The improved charge separation efficiency can be ascribed to the confinement effect of TiO_2 nanotubes.

The photocatalytic performance of the Bi_2O_3-in-TNTs with different Bi_2O_3 loadings was assessed with the results presented in Figure S3. Compared to the bare TNTs, the TNTs with Bi_2O_3 inside demonstrated improved visible light catalytic performance toward MO degradation (Figure S3). This is ascribed to visible light harvesting by the Bi_2O_3 component (Fig. 5). The degradation rate reached its climax at the Bi_2O_3 percentage of 2.0 wt%, after which further increase of Bi_2O_3 led to slower degradation performance. A comparison of the photocatalytic performances between Bi_2O_3-in-TNTs and Bi_2O_3-out-TNTs is shown in Fig. 7a. The Bi_2O_3 amount is 2.0 wt% for both catalysts. The removal percentages of MO after 180 min irradiation by Bi_2O_3-in-TNTs and Bi_2O_3-out-TNTs were 89.6 and 52.5%, respectively, and the experimental error was within 5%. The Bi_2O_3-in-TNTs exhibited better photocatalytic performance than Bi_2O_3-out-TNTs. In addition, the Bi_2O_3-in-TNTs demonstrated pretty good long-term stability and recycling

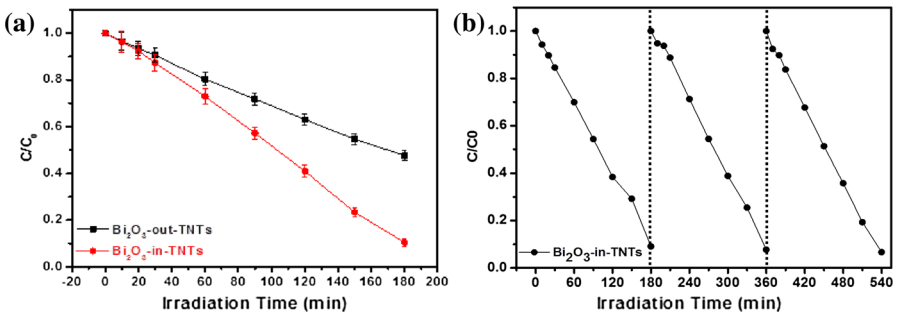

Fig. 7 **a** Photocatalytic degradation of MO over Bi_2O_3-in-TNTs and Bi_2O_3-out-TNTs under visible light irradiation; **b** repeated degradation of MO over Bi_2O_3-in-TNTs

performance, with no decay of photocatalytic activity over three successive MO degradation experiments (Fig. 7b). Reference tests show that photolysis and adsorption cannot cause the degradation of MO (Figure S5 and S6), and the degradation rate of P25, TNTs and commercial Bi_2O_3 is 6.6, 13.5 and 24.6% at 180 min of irradiation (Figure S4 and S6). The reason for low photocatalytic performance of commercial Bi_2O_3 may be that conduction band electrons and valence band holes are easily recombined when commercial Bi_2O_3 is irradiated by visible light.

The active species for photocatalytic MO degradation on Bi_2O_3-in-TNTs was investigated by using *p*-benzoquinone (BQ) and *t*-butanol (TBA) as the sacrificial agents for superoxide radicals ($\cdot O_2^-$) and hydroxyl radicals (·OH), respectively [29]. Photodegradation rate was much suppressed with the addition of BQ in the suspension (Fig. 8a), while in presence of hole scavenger TBA, the degradation rate was only halved (Fig. 8a). This phenomenon indicates both $\cdot O_2^-$ and ·OH are responsible for the MO photodegradation on Bi_2O_3-in-TNTs, but $\cdot O_2^-$ radicals act more efficiently toward MO degradation on Bi_2O_3-out-TNTs' surface (Fig. 8b).

MO degradation mechanism on Bi_2O_3-in-TNTs is illustrated in Scheme 1. The advantageous catalytic activity of Bi_2O_3-in-TNTs originates from its unique structure of an electron-deficient interior surface and an electron-enriched exterior surface, which is similar to CNTs [30–32] and is proven by the XPS spectra and H_2-TPR. Owing to the electron-deficient property of the inner surface of TNTs, it is reasonable that photo-generated electrons and holes are more easily separated. Due to the improvement of the charge separation effect, the photogenerated carriers' recombination is reduced (supported by the EIS results). Thus, ·OH radicals can be formed by combination of OH^- with holes at the Bi_2O_3 surface, while $\cdot O_2^-$ radicals are generated when photo-generated electrons combined with oxygen molecules in solution. It is important to mention that the ·OH radicals were generated mainly when Bi_2O_3 nanoparticles were confined with TiO_2 nanotubes (Fig. 8). These ·OH and $\cdot O_2^-$ radicals act synergistically toward MO decomposition, but in different regions. The confinement of TiO_2 nanotubes in Bi_2O_3-in-TNTs is responsible for its superior MO photodegradation performance over Bi_2O_3-out-TNTs.

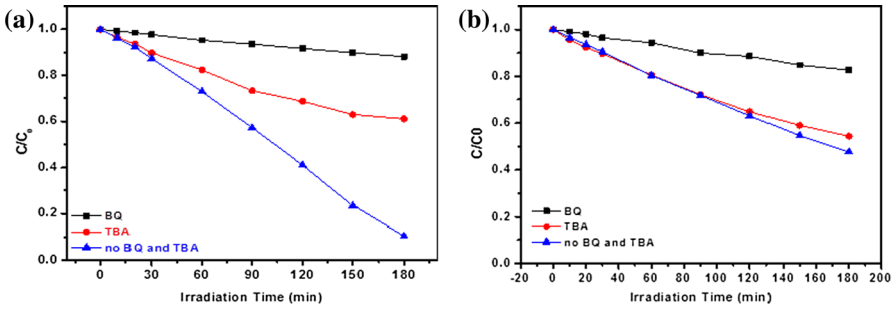

Fig. 8 Photocatalytic degradation of MO over **a** Bi_2O_3-in-TNTs and **b** Bi_2O_3-out-TNTs in presence of BQ and TBA

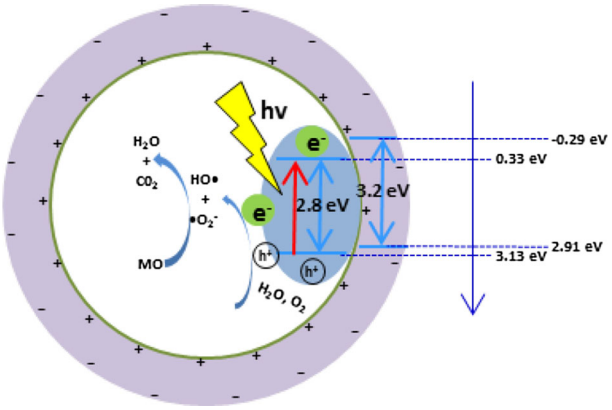

Scheme 1 The schematic illustration of MO degradation mechanism on Bi_2O_3-in-TNTs

Conclusions

In summary, Bi_2O_3 nanoparticles confined in TiO_2 nanotubes (Bi_2O_3-in-TNTs) were successfully synthesized via a vacuum-assisted method. The material was fully characterized by SEM, TEM, XRD, XPS, and H_2-TPR. The XPS and H_2-TPR measurements revealed that the Bi_2O_3-in-TNTs was electron-deficient inside the tubes. MO degradation experiments showed Bi_2O_3-in-TNTs exhibited better visible light-driven MO photodegradation performance than Bi_2O_3-out-TNTs, which is ascribed to the confinement effect of the TiO_2 nanotubes. Further degradation mechanisms disclosed $\cdot O_2$ radicals are the major oxidant species taking part in the decomposing process. The high photocatalytic activity of the confined Bi_2O_3 catalyst suggests its potential as a promising catalyst for the removal of environmental pollutants by utilization of sun light.

Acknowledgements This study was funded by Science and Technology Program of Guangzhou, China (No. 201803030019) and the Natural Science Foundation of Guangdong Province (No. 2015A030313715). G.P. thanks the partial support of Natural Science Foundation of Jiangxi Province (20171BAB213010). The authors thanks for the support from the Analytical & Testing Center, Guangzhou Institute of Energy Conversion, Chinese Academy of Sciences, China. The authors declare that there is no conflict.

References

1. S. Kumar, A. Kumar, A. Bahuguna, V. Sharma, V. Krishnan, Beilstein. J. Nanotechnol. **8**, 1571 (2017)
2. P. Verma, S.K. Samanta, Res. Chem. Intermed. **43**, 11 (2017)
3. L.P. Wu, M.Y. Zhang, J. Li, C.Q. Cen, X.J. Li, Res. Chem. Intermed. **42**, 5 (2015)
4. H. Yu, J. Wang, S. Zhang, X.J. Li, H.J. Zhao, Chin. Sci. Bull. **56**, 23 (2011)
5. G.M. Peng, R. Du, Q.M. Peng, S.Q. Wu, C.L. Yu, Mater. Chem. Phys. **214**, 34 (2018)
6. L. Ren, Y.Z. Li, J.T. Hou, J.L. Bai, M.Y. Mao, M. Zeng, X.J. Zhao, N. Li, Appl. Catal. B Environ. **181**, 625 (2016)

7. H.Q. Sun, R. Ullah, S. Chong, H.M. Ang, M.O. Tade, S.B. Wang, Appl. Catal. B Environ. **108**, 1 (2011)
8. N.C. Greenham, X.G. Peng, A.P. Alivisatos, Phys. Rev. B **54**, 24 (1996)
9. L. Li, P.A. Salvador, G.S. Rohrer, Nanoscale **6**, 1 (2014)
10. Y. Cheng, F. Gao, L. An, J. Lan, X.M. Li, G.H. Wang, Res. Chem. Intermed. **41**, 3 (2015)
11. G. Peng, J. Wu, S. Wu, X. Xu, J.E. Ellis, G. Xu, A. Star, D. Gao, J. Mater. Chem. A **4**, 1520 (2016)
12. M.L. Chang, H. Hu, Y. Zhang, D. Chen, L.P. Wu, X.J. Li, Nanomater (Basel) **7**, 5 (2017)
13. D.F. Xu, Y. Hai, X.C. Zhang, S.Y. Zhang, R.G. He, Appl. Surf. Sci. **400**, 530 (2017)
14. M. Malligavathy, S. Iyyapushpam, S.T. Nishanthi, D. Pathinettam Padiyan, J. Nanoparticle Res. **19**, 4 (2017)
15. J.S. Chen, S.Y. Qin, Y.D. Liu, F. Xin, X.H. Yin, Res. Chem. Intermed. **40**, 2 (2014)
16. L. An, G.H. Wang, Y. Cheng, L. Zhao, F. Gao, Y. Tian, Res. Chem. Intermed. **41**, 10 (2015)
17. W. Chen, X. Pan, M.G. Willinger, D.S. Su, X.H. Bao, J. Am. Chem. Soc. **128**, 10 (2006)
18. W. Chen, X. Pan, X.H. Bao, J. Am. Chem. Soc. **129**, 23 (2007)
19. X. Pan, X.H. Bao, Acc. Chem. Res. **44**, 8 (2011)
20. X. Yang, L.P. Wu, L.L. Ma, X.J. Li, T.J. Wang, S.J. Liao, Catal. Commun. **59**, 184 (2015)
21. X. Yang, X. Yu, L.Z. Long, T.J. Wang, L.L. Ma, L.P. Wu, Y. Bai, X.J. Li, S.J. Liao, Chem. Commun. **50**, 21 (2014)
22. W.B. Wang, M.Y. Ding, L.L. Ma, X. Yang, J. Li, N. Tsubaki, G.H. Yang, T.J. Wang, X.J. Li, Fuel **164**, 347 (2016)
23. X. Yang, X.Y. Lu, L.P. Wu, J.F. Zhang, Y.Q. Huang, X.J. Li, Environ. Chem. Lett. **15**, 3 (2017)
24. S. Zhang, W.M. Luo, X. Yang, T. Lv, Y.Q. Huang, K.J. Dong, X.J. Li, Chem. Select. **2**, 16 (2017)
25. L.Z. Long, X. Yu, L.P. Wu, J. Li, X.J. Li, Nanotechnology **25**, 3 (2014)
26. L.P. Wu, Y. Qiu, M. Xi, X.J. Li, C. Chen, New J. Chem. **39**, 6 (2015)
27. W.Y. Gou, P. Wu, D.M. Jiang, X.M. Ma, J. Alloy. Compd. **646**, 437 (2015)
28. H. Yu, X.J. Li, S.J. Zheng, W. Xu, Mater. Chem. Phys. **97**, 1 (2006)
29. E.M. Rodríguez, G. Márquez, M. Tena, P.M. Álvarez, F.J. Beltrán, Appl. Catal. B Environ. **178**, 45 (2015)
30. R.C. Haddon, Science **261**, 5128 (1993)
31. P.W. Leu, B. Shan, K. Cho, Phys. Rev. B **73**, 19 (2006)
32. D. Ugarte, A. Chatelain, W.A.D. Heer, Science **274**, 5294 (1996)